crystals

MDPI

Article

Growth of β-Ga_2O_3 Single-Crystal Microbelts by the Optical Vapor Supersaturated Precipitation Method

Yongman Pan [1,2,3], Qiang Wang [4], Yinzhou Yan [1,2,3], Lixue Yang [5], Lingyu Wan [6], Rongcheng Yao [6] and Yijian Jiang [1,2,3,*]

1 Institute of Laser Engineering, Faculty of Materials and Manufacturing, Beijing University of Technology, Beijing 100124, China; panym@emails.bjut.edu.cn (Y.P.); yyan@bjut.edu.cn (Y.Y.)
2 Institute of Matter Science, Beijing University of Technology, Beijing 100124, China
3 Key Laboratory of Trans-Scale Laser Manufacturing Technology, Beijing University of Technology, Ministry of Education, Beijing 100124, China
4 College of New Materials and Chemical Engineering, Beijing Institute of Petrochemical Technology, Beijing 102617, China; qwang@bipt.edu.cn
5 School of Printing and Packing Engineer, Beijing Institute of Graphic Communication, Beijing 102627, China; yanglixue@bigc.edu.cn
6 School of Physical Science and Technology, Guangxi University, Nanning 530004, China; wanlingyu75@126.com (L.W.)
* Correspondence: yjjiang@bjut.edu.cn

Abstract: Monoclinic β-Ga_2O_3 microbelts were successfully fabricated using a one-step optical vapor supersaturated precipitation method, which exhibited advantages including a free-standing substrate, prefect surface, and low cost. The as-grown microbelts possessed a well-defined geometry and perfect crystallinity. The dimensions of individual β-Ga_2O_3 microbelts were a width of ~50 μm, length of ~5 mm, and thickness of ~3 μm. The SEM, XRD, HRTEM, XPS, and Raman spectra demonstrated the high single-crystalline structure of β-Ga_2O_3 microbelts. Twelve frequency modes were activated in Raman spectra. The optical band gap of the β-Ga_2O_3 microbelt was calculated to be ~4.45 eV. Upon 266 nm excitation, 2 strong UV emissions occurred in photoluminescence spectra through the radiative recombination of self-trapped excitons, and the blue emission band was attributed to the presence of donor-acceptor-pair transition. The individual β-Ga_2O_3 microbelt was employed as metal-semiconductor-metal deep-ultraviolet photodetector, which exhibits the photoresponse under 254 nm. This work provides a simple and economical route to fabricate high-quality β-Ga_2O_3 single-crystal microbelts, which should be a potential synthetic strategy for ultra-wide bandgap semiconductor materials.

Keywords: β-Ga_2O_3; microbelts; OVSP; photoluminescence; photoconductivity

check for updates

Citation: Pan, Y.; Wang, Q.; Yan, Y.; Yang, L.; Wan, L.; Yao, R.; Jiang, Y. Growth of β-Ga_2O_3 Single-Crystal Microbelts by the Optical Vapor Supersaturated Precipitation Method. *Crystals* **2023**, *13*, 801. https://doi.org/10.3390/cryst13050801

Academic Editor: Francisco M. Morales

Received: 7 April 2023
Revised: 1 May 2023
Accepted: 8 May 2023
Published: 10 May 2023

Copyright: © 2023 by the authors. Licensee MDPI, Basel, Switzerland. This article is an open access article distributed under the terms and conditions of the Creative Commons Attribution (CC BY) license (https://creativecommons.org/licenses/by/4.0/).

1. Introduction

Deep-ultraviolet (DUV) photodetectors that operate in the solar-blind spectrum range (190–280 nm) have attracted much attention due to their potential applications in various fields such as missile warning, biochemical detection, and security communication [1–3]. These applications have been demonstrated in semiconductor materials with various device architectures, including ultraviolet enhanced Si-based photodiodes [4], ZnO [5], diamond [6], AlN [7], and AlGaN [8]. Nevertheless, currently available Si-based DUVs require optical filters to block out visible and infrared light, leading to the low penetration depth of high-energy UV photons. Moreover, the high-defect density and complex alloying process in alloy wide bandgap semiconductors can affect the high-quality epitaxy, cut-off wavelength, and signal-noise ratio, etc. As an alternative, monoclinic β-Ga_2O_3 is an attractive class of ultra-wide bandgap semiconductor material due to its excellent physical properties, such as suitable electronic bandgap (4.2~4.9 eV), large

breakdown electric field (8 MV/cm) [9,10], and superior room-temperature PL. Furthermore, β-Ga_2O_3 exhibits high optical transparency in both the DUV and visible wavelength regions, which makes it a promising candidate for exploring DUV photodetectors [11]. These distinct properties offer an ideal platform for various unique civil and military applications. To date, several morphologies, including bulk, epitaxial layers, and micro-/nanostructures have been demonstrated on β-Ga_2O_3-based optoelectronic devices. Among them, micro-/nanostructures with a large amount of multiformity, large surface-to-volume ratio, and shorter effective conductive channels were considered an ideal system for investigating dimensionally confined carrier transport phenomena, as well as building blocks for optoelectronic devices. Therefore, it would be greatly advantageous and attractive to explore novel desirable solar-blind photodetectors via an easy fabrication process and low-cost strategy.

Well-established techniques of physical evaporation [12,13], thermal evaporation [14,15], and chemical vapor deposition (CVD) [16–18] have been carried out to fabricate abundant β-Ga_2O_3 structures including nanowires, nanobelts, and microwires. Several studies have reported the achievement of preparing β-Ga_2O_3 micro-/nanostructures. The β-Ga_2O_3 nanowires have been grown using a thermal evaporation method, in which metallic gallium was placed on the substrate formed by compact powders of Ga_2O_3 and then sintered at a high temperature of 1150 °C for 8 h [19]. The growth time of β-Ga_2O_3 nanowires was shortened to 3 h through the metal-assist multistep process [20]. Although the catalyst-free CVD method could be applied to fabricate the β-Ga_2O_3 microbelt in 30 min, the complex process of inductively coupled plasma dry etching on sapphire substrate was required [21]. Similarly, the β-Ga_2O_3 microwires could be synthesized in 30 min, for which the clean silicon substrate needed to be covered with 100 nm β-Ga_2O_3 film as a buffer layer [22]. Therefore, the sophisticated fabrication processes in the above techniques limit the development of the practical routes; for example, the time-consuming growth process lowers the growth efficiency, the complexity of the fabricating procedure for the substrate increases the cost, and the metal-assisted catalytic method can lead to the unintentional doping of the β-Ga_2O_3 to form deep-level impurities inside the micro-/nanostructures. Compared with these approaches, the one-step optical vapor supersaturated precipitation (OVSP) method, which was able to adjust the gas flux, growth time, growth power, and other parameters during the growing process in real time, was impressive [23–26]. During the OVSP process, the growth driving force is based on vapor supersaturated precipitation in the homogeneous temperature field, which is conducive to avoiding the generation of compensation defects. This is obviously different from the previous studies where temperature gradients were used as the growth driving force [27,28], which may lead to thermal-fluctuation-induced lattice mismatching. Moreover, the quasi-equilibrium OVSP method was free of substrate, which could further improve the crystallinity of micro-/nanostructures and reduce cost.

Controlling the dimensionality and crystal quality of β-Ga_2O_3 micro-/nanostructures is not only synthetically interesting, but also could promote the practical application of ultra-wide bandgap semiconductor photodetectors. The optical properties of β-Ga_2O_3 mainly focus on spectroscopic identification of the carrier trapped by intrinsic defects, which were crucial to influencing the carrier concentrations or acting as recombination centers [29,30]. Typical photoluminescence (PL) spectra of β-Ga_2O_3 are acknowledged to be in UV and blue (BL) bands [31,32]. The UV band is traditionally recognized as being impurity-independent, and experiments accompanied by theoretical studies have attributed this to the recombination of a self-trapped exciton (STE) from the free electrons to the self-trapped hole (STH) states [33]. The BL band originates from the donor-acceptor-pair (DAP) recombination [34]. These emission properties could be affected by the deep-level defects. A variety of defect features that vary with growth and processing have been reported, but the specific defect origins of PL bands in β-Ga_2O_3 is still a controversial topic. Further investigation is needed to correlate the photoelectric performance with intrinsic defects.

In this work, we proposed a one-step OVSP method for the fabrication of high-quality β-Ga_2O_3 microbelts with a free-standing substrate. The growth mechanism of β-Ga_2O_3 microbelts was revealed, which depended on a quasi-equilibrium process supported by a uniformed temperature field originating from the homogeneous optical heating zone, rather than temperature gradients. The SEM, XRD, HRTEM, and XPS spectra demonstrated the high single-crystalline structure of β-Ga_2O_3 microbelts. The optical and electrical properties of a single β-Ga_2O_3 microbelt were demonstrated. The optical band gap of the β-Ga_2O_3 microbelt was calculated to be ~4.45 eV. Upon 266 nm excitation, two strong UV and blue emission bands were attributed to the radiative recombination of STE and DAP transition, respectively. The β-Ga_2O_3 microbelt exhibited photoresponse at 254 nm illumination. This work provides a facile approach to prepare high-quality β-Ga_2O_3 microbelts for a variety of optoelectronic applications in micro/nanophotonics.

2. Experimental Section

2.1. Fabrication of β-Ga_2O_3 Microbelts

The mixture of Ga_2O_3 (Alfa Aesar, Ward Hill, MA, USA, 99.999%) and graphite powders with a weight ratio of 1:1 was pressed by isostatic pressing at 68 MPa for 30 min as a reactive precursor rod, the dimensions of which were ~6 mm in diameter and ~3 cm in length. The precursor rod was produced in an optical floating zone furnace (Crystal Systems Co., Ltd, 10000H–HR-I-VPO-PC, Kobuchisawa, Hokuto, Yamanashi, Japan) equipped with four of 1500 W halogen lamps. The lamp power was first increased to 52%@1500 W within 0.3 h. Then the lamp power was held for 0.5 h for the growth of β-Ga_2O_3 microbelts using the OVSP method. Finally, the power was reduced to zero within 0.3 h to release the residual stress of the microbelts. The precursor rod was rotated at 10 rpm during OVSP growth. The carrier gas of O_2 was pumped into the chamber at 50 mL/min. As-grown β-Ga_2O_3 microbelts were cooled to the room temperature naturally.

2.2. Characterization

The morphology and elemental mapping of β-Ga_2O_3 microbelt was obtained by scanning electron microscopic (SEM, Shimadzu SSX-550, Kyoto, Japan), which was equipped with an energy-dispersive spectrometer (EDS). High-resolution transmission electron microscopy (HRTEM) was performed using JEOL JEM-F200. The TEM image of the β-Ga_2O_3 microbelt was taken from a thin edge by grinding the sample. The crystal structure was determined by X-ray diffraction (XRD) (Bruker D8 DISCOVER), which operated at 40 kV and 40 mA with a step size of 0.02° in the diffraction angle range from 20° to 80°. The Raman and PL spectra were acquired by a SmartRaman confocal-micro-Raman system (developed by Institute of Semiconductors, Chinese Academy of Sciences, Beijing, China) under the backscattering geometry. The collected Raman and PL signals were analyzed using a Horiba LabRAM iHR550 spectrometer. For Raman spectral analysis, a 633 nm He-Ne laser with linear polarization (Thorlabs, Newton, NJ, USA, HNL210) was used as the excitation source, equipped with a 2400 lines/mm grating and a $10\times/NA$ 0.25 objective (Olympus MPlan N, Shinjuku, Japan). For PL spectra acquisition, a 266 nm line CW laser (CRYTU FQCW266, Berlin, Germany) was used as the excitation source, equipped with a 600 lines/mm grating and a $20\times/NA$ 0.40 objective (Thorlabs, LMU-20×-UVB). X-ray photoelectron spectroscopic (XPS) analysis was conducted using a photoelectron spectrometer (Thermo Fisher Scientific, Waltham, MA, USA, ESCALAB 250Xi) with monochromatic Al-Kα radiation. The binding energies were then calibrated using the C 1s peak at 284.80 eV to compensate for the surface charges. The ultraviolet-visible (UV-vis) absorption spectrum was recorded by an UV-vis spectrophotometer (UV-3600IPLUS, Shimadzu, Kyoto, Japan), in which the $BaSO_4$ powder was used as the reference.

2.3. Device Construction

The configuration of the photodetector was based on a single microbelt with (In/Ga)/β-Ga_2O_3/(In/Ga) as the metal-semiconductor-metal (MSM) DUV structure. The In/Ga elec-

trodes were fabricated using a manual droplet deposition technique. Firstly, the β-Ga_2O_3 microbelt was transferred onto a cleaned glass substrate. Then, a needle tube was employed to carefully deposit In/Ga electrodes, approximately 1 mm in diameter, onto both ends of the β-Ga_2O_3 microbelt to establish ohmic contacts. The distance between the In/Ga electrodes was approximately 267 μm, as determined by an optical microscope. The effective working area of the β-Ga_2O_3 microbelt-based DUV detector was measured to be 1.4×10^{-4} cm^2. The current-voltage (*I*-*V*) curves were measured by a source meter (Keithley, Cleveland, OH, USA, SMU 2600B) equipped with a tip-probe platform and the Auto Curve Analysis Tracer Software v. 2.1.4. The photoresponse curve of the photodetector was recorded using a Xenon lamp with a monochromator sorting filter. All the characterizations and measurements were performed at room temperature and ambient conditions. The standard undoped *n*-β-Ga_2O_3 single crystal bulk (purchased from Hefei Kejing Material Technology Co., Ltd., Anhui, China) with orientation of <100> was used as control, of which the size was $10 \times 10 \times 0.5$ mm^3.

3. Results and Discussion

3.1. Growth of β-Ga_2O_3 Microbelts

Figure 1a shows a schematic diagram of the OVSP process for β-Ga_2O_3 microbelt growth. The growth was carried out in a quartz chamber with controllable gas atmospheres. Light from four halogen lamps was focused on the chamber center by ellipsoidal mirrors in order to form a homogenized optical heating zone, where the Ga_2O_3 precursor rod was positioned and rotated for uniformed heating. Figure 1b demonstrates the imaged OVSP growth process of β-Ga_2O_3 microbelts, which can be divided into two stages. In the first growth stage, cracks emerged in the surface of the precursor rod, accompanied by volatile white smoke, which originated from the decomposition of Ga_2O_3 into Ga_2O and *Ga* vapors through the carbothermal reduction reaction. When the growth temperature was greater than the threshold for β-Ga_2O_3 microbelts, the concentrations of Ga_2O and *Ga* vapors were dramatically increased. In the second stage, the Ga_2O and *Ga* vapors were supersaturated and deposited directly on the precursor rod with a Ga_2O_3 crystal nucleus to form a belt-like architecture. Finally, hundreds of free-standing transparent individual Ga_2O_3 microbelts were obtained from the cluster architectures on the precursor rod. The growth mechanism of Ga_2O_3 microbelts can be specified as:

$$2Ga_2O_3 + 5C \rightarrow Ga_2O + 2Ga + 5CO \quad (1)$$

$$Ga_2O + O_2 \rightarrow Ga_2O_3 \quad (2)$$

$$4Ga + 3O_2 \rightarrow 2Ga_2O_3 \quad (3)$$

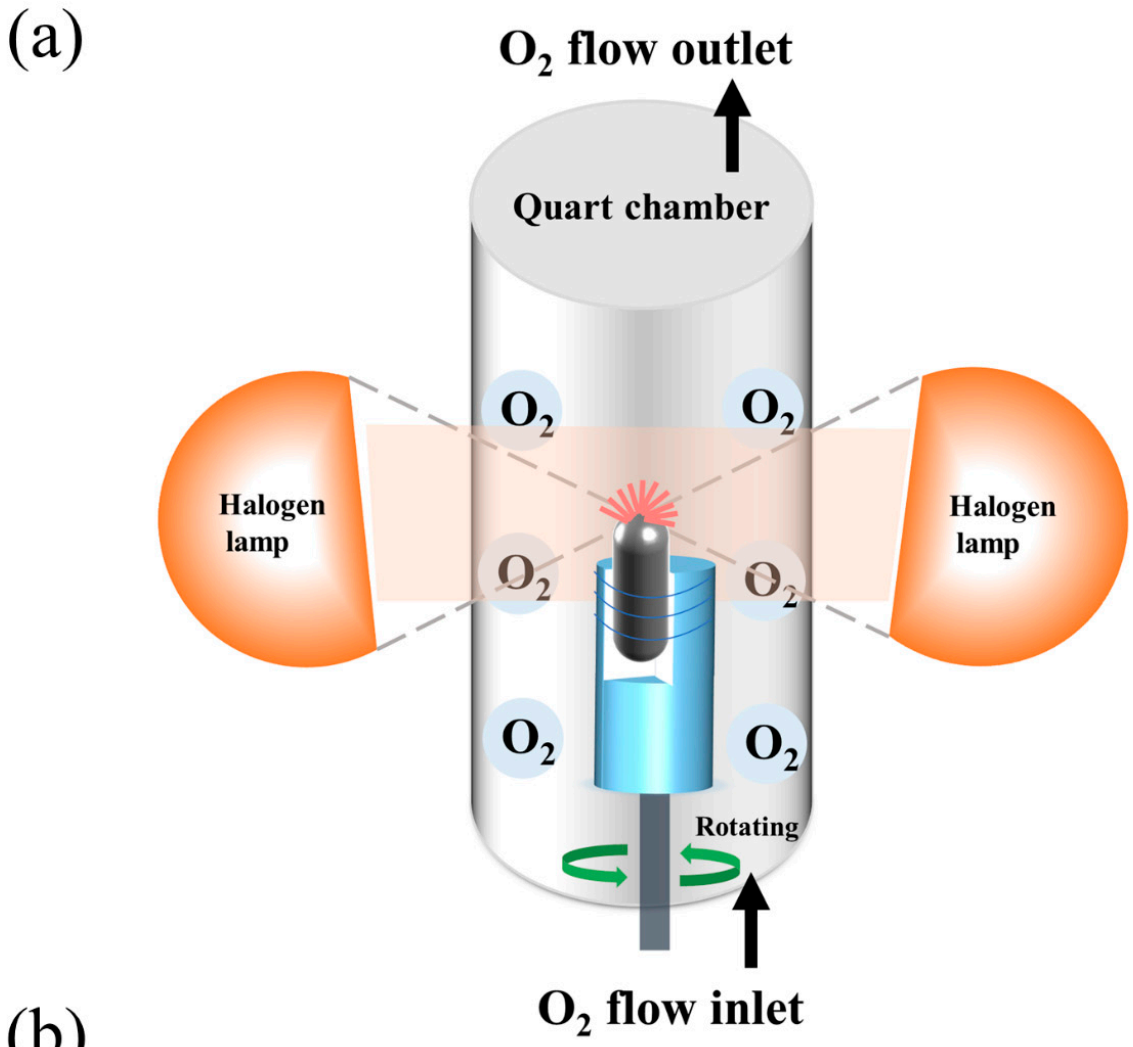


Figure 1. (**a**) Schematic diagram of the optical floating zone furnace; (**b**) evolution of the growth process for Ga_2O_3 microbelts.

3.2. Microstructures of β-Ga_2O_3 Microbelts

Figure 2a shows the typical optical and SEM images of an individual β-Ga_2O_3 microbelt. The β-Ga_2O_3 microbelts were rectangular with a width of ~50 μm and a length of ~5 mm. The thickness of about 3 μm indicated the belt-like architecture of β-Ga_2O_3 microbelts grown by OVSP, as captured in the lower left inset of Figure 2a. The repeatability was verified by the process of multiple growths of β-Ga_2O_3 microbelts under the same optimum conditions. The distribution of diameter (w) measured from 36 microbelts is shown in the upper right inset of Figure 2a, where w = 52 ± 15 nm. The EDS mapping spectra demonstrated the uniform spatial distribution of the Ga and O elements, as shown in Figure 2b. Elements C and Au in the EDS spectrum were assigned to the specimen holder. Figure 2c shows the periodic atomic arrangement of the β-Ga_2O_3 microbelt captured by HRTEM. The well-resolved lattice fringes of 0.297 nm corresponded to the (400) plane [35]. The fast Fourier transition (FFT) pattern taken from the HRTEM image clearly showed the symmetrical sharp diffraction spots, indicating the single-crystal microstructure of the β-Ga_2O_3 microbelt, as shown in the inset in Figure 2c [36]. Figure 2d shows the vertical XRD pattern of an individual β-Ga_2O_3 microbelt, where the growth orientation of the microbelt was placed perpendicularly along the X-ray, as shown in the inset of Figure 2d. All diffraction peaks were indexed as the monoclinic-type structure (JCPDS No. 43-1012). Three dominant peaks located at 30.03°, 45.77°, and 62.45°; corresponded to (400), (600), and (800) crystal planes, respectively. The full width of half peak (FWHM) of the (400) plane was estimated to be ~0.06°, which was ~1.9-fold narrower than that previously reported by Shen et al., indicating the high quality of the β-Ga_2O_3 microbelt [37]. The average crystallite size (D) was calculated using the Scherrer equation:

$$D = \frac{0.89\lambda}{\beta\cos\theta} \quad (4)$$

where λ is the X-ray wavelength of 0.15406 nm, β and θ are the FWHM and diffraction angle of the (400) peak, respectively [38]. The D of β-Ga_2O_3 microbelts was calculated to be 136 nm.

Figure 3a illustrates the micro-Raman spectra of an individual β-Ga_2O_3 microbelt in the temperature range of 300 K to 120 K. The room-temperature Raman spectrum of a standard β-Ga_2O_3 bulk single crystal was set as control. The low-frequency Raman active modes (R1: 113, 144, 169, 200 cm^{-1}) were assigned to the vibration and translation of the tetrahedra-octahedra chains, the mid-frequency modes (R2: 320, 346, 417, 476 cm^{-1}) were attributed to the deformation of Ga_2O_6 octahedra, and the high-frequency modes (R3: 630, 653, 659, 767 cm^{-1}) were related to the stretching and bending phonon frequencies of Ga_1O_4 tetrahedra, respectively [39]. When the temperature increased from 120 K to 300 K, the Raman shift and FWHM of the mode at A_{g10} (767 cm^{-1}) exhibited a linear variation, including a blueshift of ~3 cm^{-1} and a FWHM widening of~2 cm^{-1}, which was attributed to the phonon-phonon interaction under the effect of temperature [40,41], as shown in Figure 3b. Table 1 summarizes the position of Raman peaks in this work and previous work reported by Dohy et al. [42]. The existence of only relatively small deviations reveals that the as-grown β-Ga_2O_3 microbelt was a monoclinic single crystal with strain and defect levels close to those of the crystalline bulk [22].

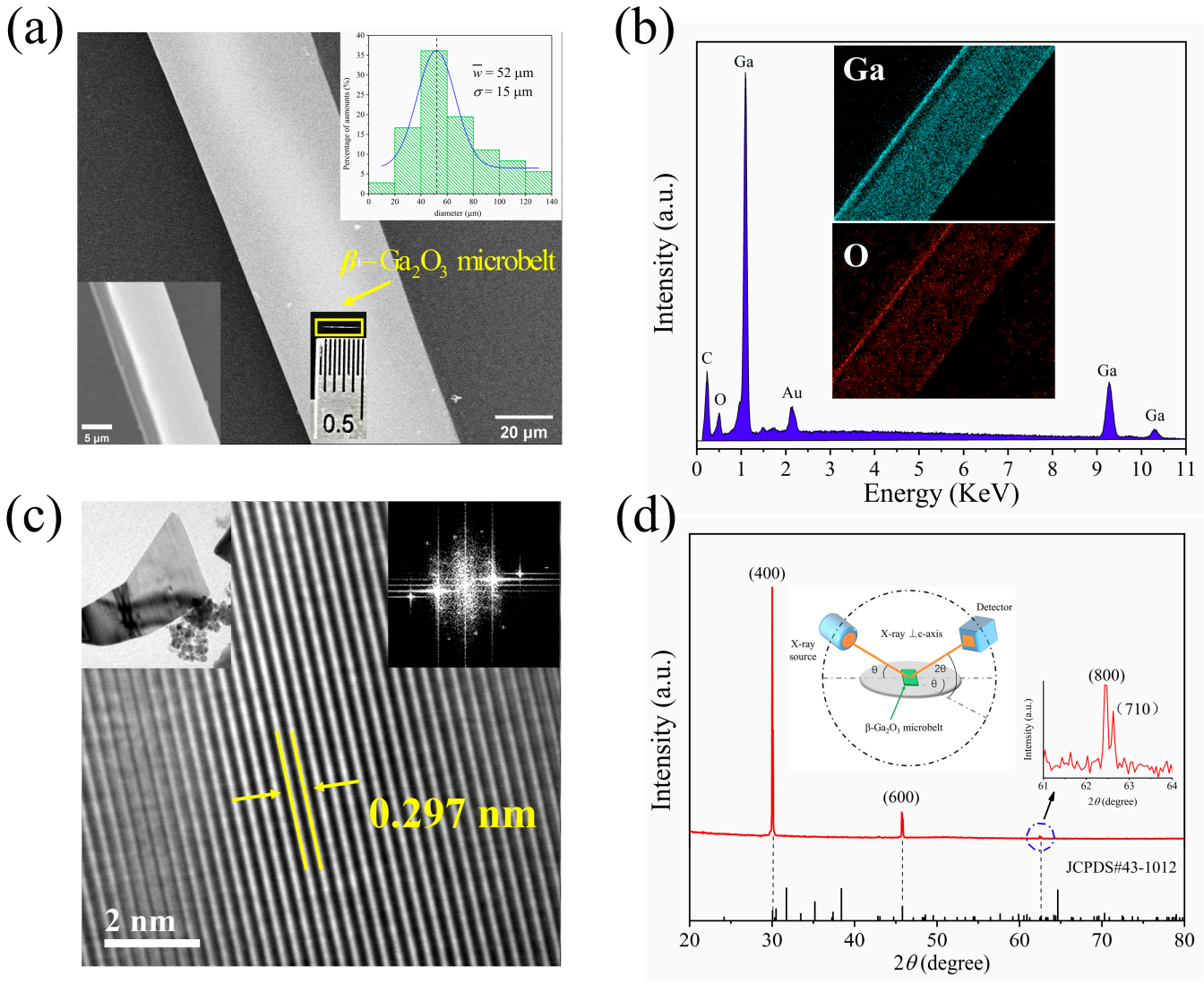


Figure 2. (**a**) The optical and SEM image of a single β-Ga_2O_3 microbelt. Inset: lower left shows a side view and upper right shows the distribution of the diameter measured from β-Ga_2O_3 microbelts. (**b**) EDS spectrum of β-Ga_2O_3 microbelt. Inset: the 2D mapping of chemical elements of Ga and O. (**c**) HRTEM image and corresponding FFT pattern of β-Ga_2O_3 microbelt. Inset: upper left shows a thin edge from grinding the microbelt for measurement. (**d**) Vertical XRD pattern of β-Ga_2O_3 microbelt. Inset: the setup of XRD measurement.

Table 1. Experimentally determined Raman modes at 300 K for the β-Ga_2O_3 microbelt.

Mode Symmetry	A_{g1}	B_{g1}	A_{g2}	A_{g3}	A_{g4}	A_{g5}	A_{g6}	A_{g7}	A_{g8}	B_{g5}	A_{g9}	A_{g10}
β-Ga_2O_3 bulk single crystal		145	169	200		346	417		630		659	767
β-Ga_2O_3 microbelt	113	144	169	200	320	346	417	476	630	653	659	767
Dohy et al.	111	147	169	199	318	346	415	475	628	651	657	763

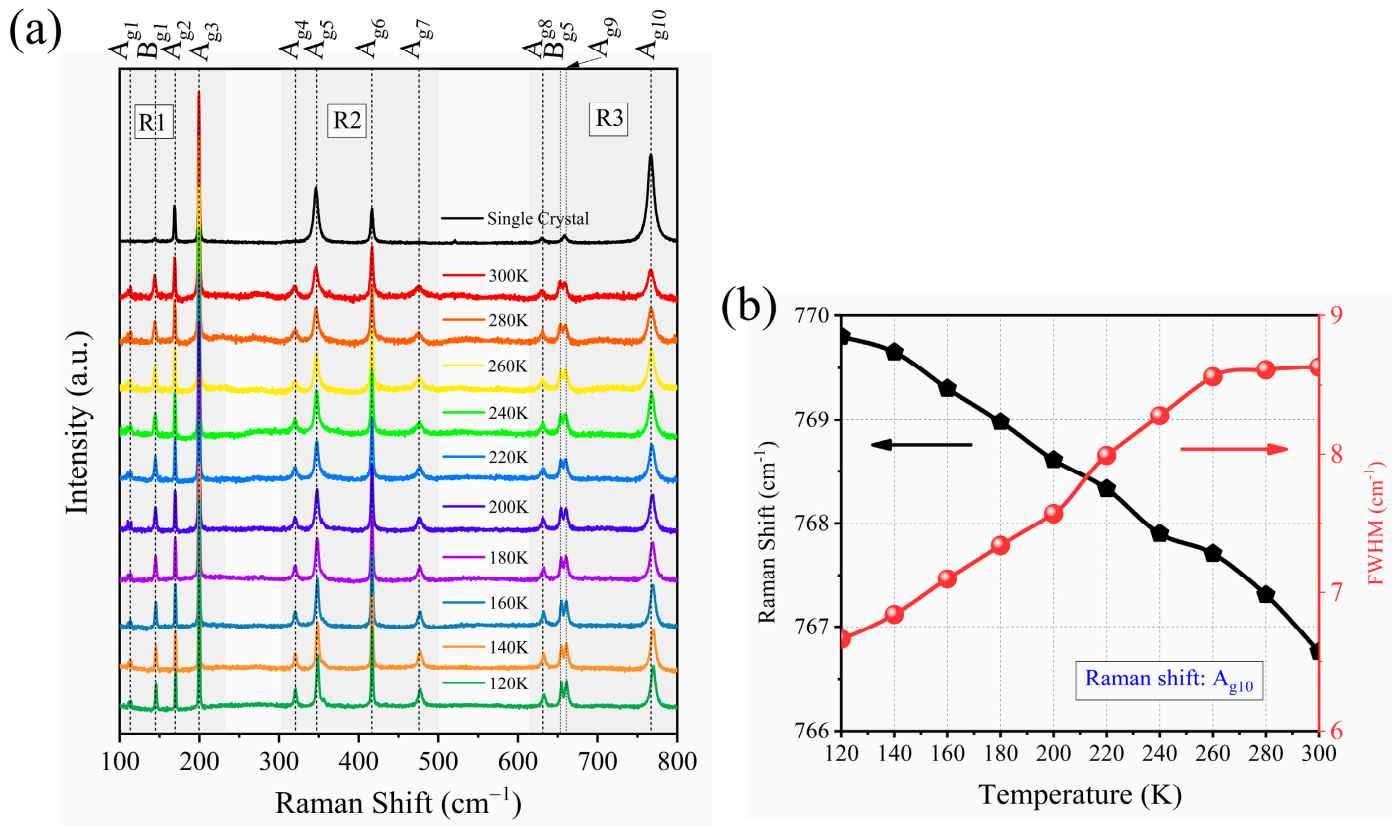


Figure 3. (**a**) The temperature-dependent micro-Raman spectra of an individual β-Ga_2O_3 microbelt. (**b**) The Raman shift of A_{g10} and corresponding temperature-dependent FWHM.

Figure 4a shows the XPS spectrum of the β-Ga_2O_3 microbelt, confirming the existence of main elements, i.e., Ga and O. As shown in Figure 4b, the two peaks of the Ga 2p spectrum were located at ~1145.9 eV and ~1119.0 eV with 26.9 eV separation, which were identified as Ga $2P_{1/2}$ and Ga $2P_{3/2}$, respectively, indicating the presentence of Ga^{3+} ions [43]. The binding energies around 20.79 eV corresponded to Ga 3d electrons [44], as shown in Figure 4c. The O 1s spectrum was fitted by two Gaussian peaks at binding energies of 531.6 eV and 532.5 eV, corresponding to the lattice oxygen (O_I) and the chemisorbed oxygen (O_{II}) [45], respectively, as shown in Figure 4d. The average Ga/O ratio in Ga_2O_3 can be estimated by the integrated intensity ratio of the deconvoluted XPS components calibrated by the relative sensitivity factor (R) using:

$$R = \frac{I_{Ga2p_{3/2}} / F_{Ga2p_{3/2}}}{I_{O1s} / F_{O1s}} \quad (5)$$

where I is the integrated intensity and F is the sensitivity factor ($F_{Ga2p3/2}$ = 2.751 and F_{O1s} = 0.733). Compared with the previously reported R value of 0.62 in β-Ga_2O_3 single crystal [46], the R value of the β-Ga_2O_3 microbelt was calculated to be 0.68, which was closer to the stoichiometric ratio of Ga_2O_3. The morphological and structural results revealed that the high-quality β-Ga_2O_3 single-crystal microbelts were grown by the OVSP method.

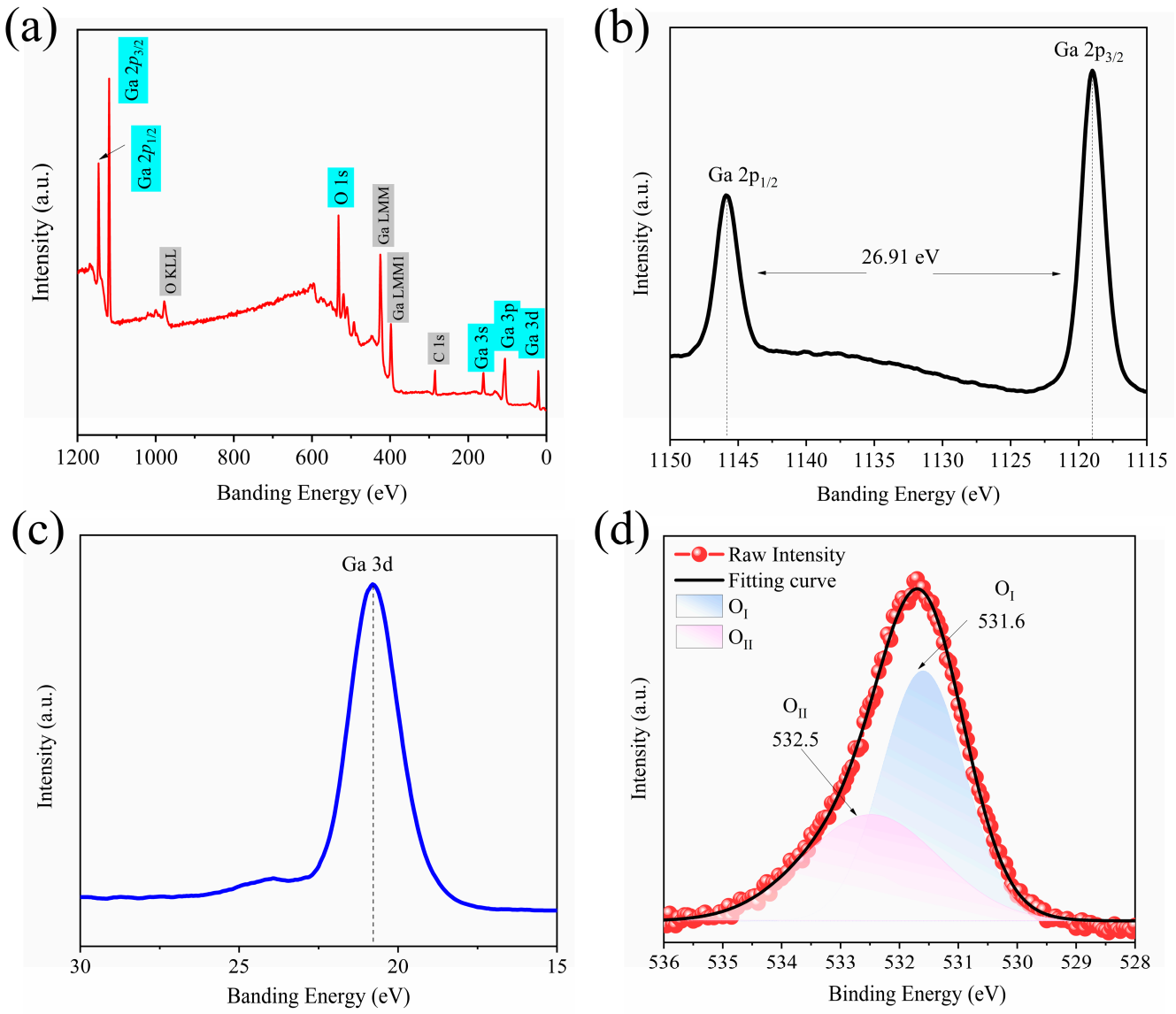


Figure 4. XPS spectra of β-Ga_2O_3 microbelt (**a**) full scan spectra: the blue mark shows the main elemental peak, the gray mark refers to Auger peak and C 1s peak, respectively; core level binding spectra of (**b**) Ga 2p, (**c**) Ga 3d, and (**d**) O 1s, respectively.

3.3. UV-Vis Absorption and PL Spectra of β-Ga_2O_3 Microbelts

Figure 5 shows the UV-vis absorption spectrum of β-Ga_2O_3 microbelts in the wavelength range of 200–700 nm. Strong absorption was observed in 200–280 nm region, indicating the ultra-wide bandgap nature of β-Ga_2O_3. The *Tauc*'s fitting was used to identify the band gap of the β-Ga_2O_3 microbelt as follows [47]:

$$\alpha h\nu = C\left(h\nu - E_g\right)^{1/2} \tag{6}$$

where α is the absorption coefficient, h is the Planck's constant, ν is the frequency of incident photon, and E_g is the optical bandgap. Plotting $(\alpha h\nu)^2$ as a function of photon energy, and extrapolating the linear portion of the curve to absorption equal to zero as shown in the inset of Figure 5, gave the E_g value of the β-Ga_2O_3 microbelt to be 4.45 eV, in good agreement with the reported value [48]. This feature makes the β-Ga_2O_3 microbelt possess the selective response to the solar-blind UV band.

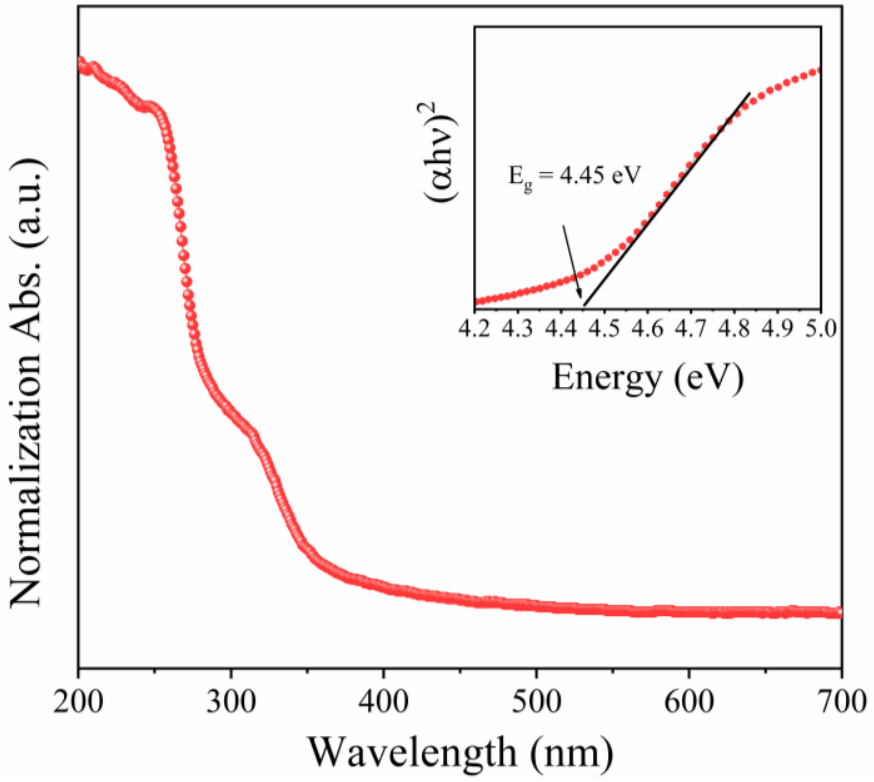


Figure 5. UV-vis absorption spectrum of the β-Ga_2O_3 microbelt. Inset: *Tauc*'s fitting of the spectrum.

Figure 6a,b shows the PL spectra of an individual β-Ga_2O_3 microbelt and the high-quality bulk β-Ga_2O_3 single crystal. The broad UV emission band of the individual β-Ga_2O_3 microbelt peak could be fitted by three Gauss peaks at 332 nm (3.73 eV, named UV-1), 368 nm (3.37 eV, named UV-2), and 402 nm (3.08 eV, named BL), which are close to those of the bulk β-Ga_2O_3 single crystal at 329 nm, 366 nm, and 403 nm respectively. The UV-1 and UV-2 emissions were attributed to the recombination of STE from the free electrons to the STH states, which were localized on the single oxygen atom in the lattice. The oxygen atom at the O I site contributed the UV-1 emission, while the one at the O II site activated the UV-2 emission [49,50]. The BL band appearing at 2.8–3.0 eV was related to the DAP transitions involving the deep donors (e.g., oxygen vacancies (V_O) and interstitial Ga) and acceptors (e.g., gallium vacancies (V_{Ga}), and V_O + V_{Ga} complexes) [51–53]. Figure 6c shows the schematic band diagram and emission behavior in the β-Ga_2O_3 microbelt. Upon 266 nm illumination, the UV-1 and UV-2 emissions occurred through the radiative recombination of STE. Meanwhile, the DAP emissions for the BL band were excited by the transition from the V_O defect to the (V_{Ga} + V_O) complex, of which the charge state was (1−), as calculated by Deák et al. [54]. The FWHM of PL emissions has been regarded as a well-accepted criterion to evaluate the crystal quality of semiconductor materials. As the temperature increased from 80 K to 300 K, the FWHM of BL emissions in the β-Ga_2O_3 microbelt and bulk β-Ga_2O_3 single crystal expanded from 88–94 nm and 83–87 nm, respectively, as illustrated in Figure 6d. The broader FWHM of β-Ga_2O_3 should be ascribed to the large Stokes shift of PL bands for optical absorption, caused by the strong electron-phonon coupling and the localization of recombining electrons and holes [55,56].

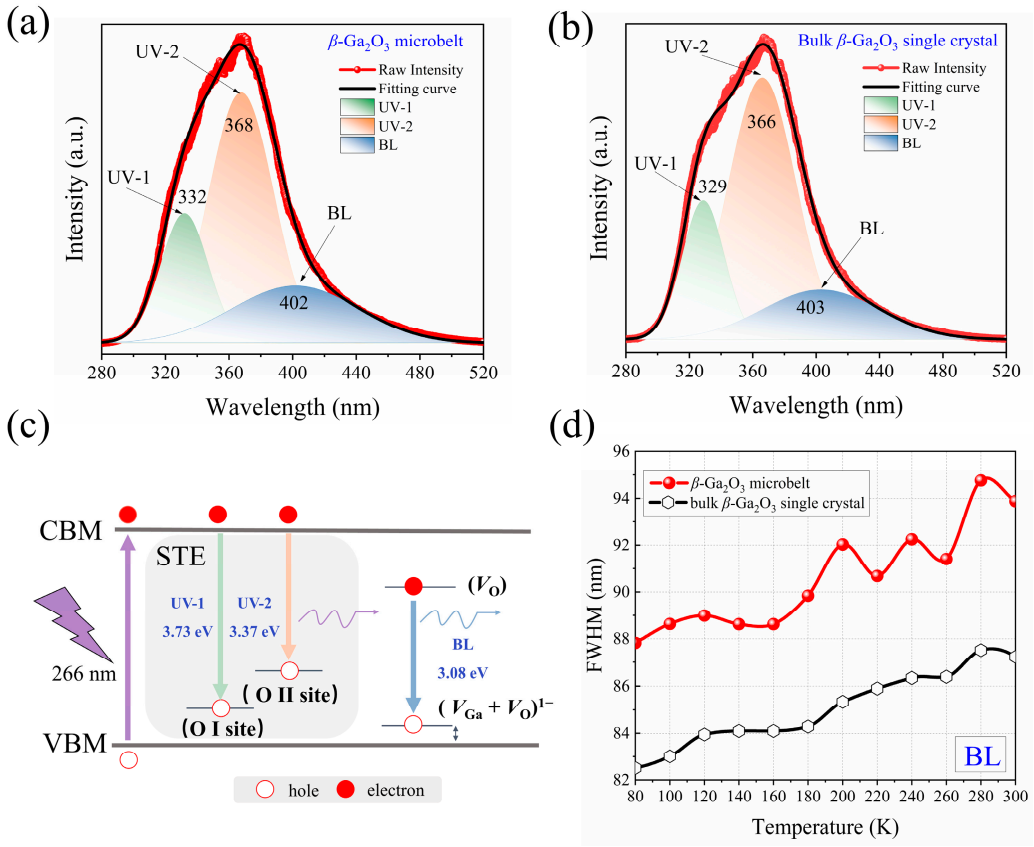


Figure 6. The PL spectra of (**a**) an individual β-Ga_2O_3 microbelt and (**b**) the high-quality bulk β-Ga_2O_3 single crystal at 300 K. (**c**) Schematic band diagram and emission behavior in the β-Ga_2O_3 microbelt. (**d**) The FWHM of BL emissions as a function of temperature in two β-Ga_2O_3 from 80 K to 300 K.

3.4. I-V Characteristics

Figure 7a illustrates the schematic of a single β-Ga_2O_3 microbelt with In/Ga electrodes, where the UV signal was illuminated (100 mW/cm^2) vertically on the MSM DUV detector. An optical microscopy image of the MSM architecture is demonstrated in the upper left of Figure 7a. The current-voltage (*I*–*V*) curves of the β-Ga_2O_3 microbelt measured under light illumination (254 nm) and in the dark are depicted in Figure 1b. The linear *I*-*V* relationships indicated ohmic contacts between In/Ga electrodes and the β-Ga_2O_3 microbelt [57]. For the belt-like architecture, the electrical resistivity (ρ) of β-Ga_2O_3 microbelt was calculated by:

$$\rho = R \times \frac{s}{l} = R \times w \tag{7}$$

where R is the resistance, s is the cross-sectional area of the microbelt, l is the length, and w is the diameter. Based on the equation, the ρ value was calculated to be $1.79 \times 10^7\ \Omega \cdot$ cm, which was in the same order of magnitude as the value reported in the previous literature [58]. Upon 254 nm illumination, the current of the MSM DUV detector increased from 5.8 nA to 7.5 nA. The positive photocurrent was attributed to the solid-state process where the photogenerated electron-hole pairs instantaneously boosted the carrier density contributing the photoconduction [29]. The responsivity (R) of the β-Ga_2O_3 photodetector under a voltage of 20 V and at a power density of 100 mW/cm^2 was calculated as follow:

$$R = \frac{I_P}{P_{UV} \times S} \tag{8}$$

where I_P was the photocurrent minus the dark current, P is power density, and S is effective illumination area. In this work, λ was 254 nm, I_λ was 7.5×10^{-9} A, I_d was

5.8 × 10^{-9} A, and S was 1.4 × 10^{-4} cm^2. The calculated R value was found to be 0.12 mA/W, which is comparable to the R value reported in previous studies on β-Ga_2O_3-based DUV photodetectors [59]. The inset of Figure 7b presents the stability characteristics of the β-Ga_2O_3 microbelt at room temperature. After the stability of 100 s, no obvious degradation was found. However, the rejection ratio of our β-Ga_2O_3 photodetector is lower than that reported in the literature [60]. One possible approach is to optimize the synthesis parameters of the β-Ga_2O_3 microbelts to enhance their crystalline quality and minimize defects, which may improve the UV performance of the photodetectors. Another approach is to modify the device structure, such as by introducing the functional layer, to improve the separation efficiency of photogenerated charge carriers and enhance the rejection ratio. These efforts will lead to improvements in the performance of the β-Ga_2O_3 photodetector, and a discussion of solutions will certainly be included in our future works. Because of the resulting photoelectric properties and the easy fabrication process, the OVSP method is a promising tool for preparing ultra-wide bandgap semiconductor materials in future optoelectronic system applications.

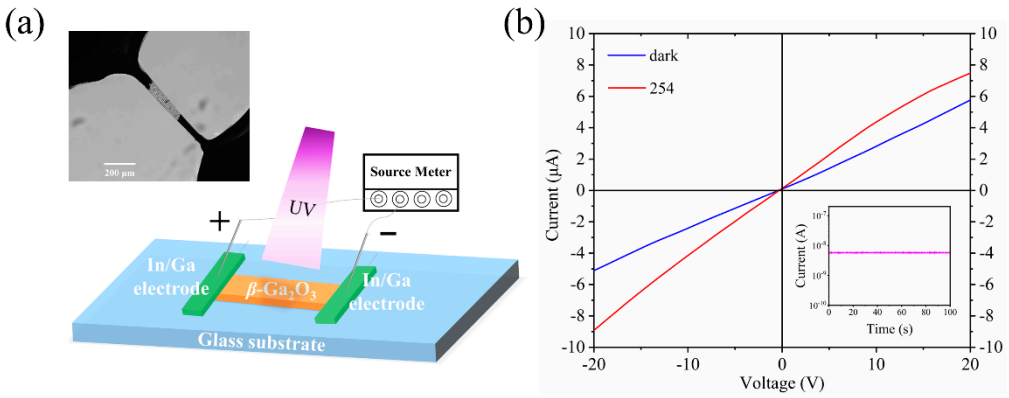


Figure 7. (**a**) The schematic illustration of individual β-Ga_2O_3 microbelt MSM architecture; the upper shows an optical microscopy image of the as-fabricated device. (**b**) The *I-V* characteristics of the device under dark and 254 nm light illumination, respectively. Inset: stability characteristic.

4. Conclusions

The β-Ga_2O_3 microbelts were grown by the OVSP method. The vapor supersaturated precipitation and uniformed temperature field provided the growth driving force, which is key to the growth process of β-Ga_2O_3 microbelts. The structural investigations of SEM, XRD, HRTEM, XPS and Raman spectra demonstrated the single-crystal character of the β-Ga_2O_3 microbelts. Twelve active frequency modes were observed in Raman spectra. With the temperature increasing, the Raman shift and FWHM of the mode at A_{g10} exhibited a redshift of ~3 cm^{-1} and a FWHM widening of~2 cm^{-1}, respectively. The optical band gap of the β-Ga_2O_3 microbelt was found to be ~4.45 eV. Two strong UV emissions and blue emissions in the PL spectra could be attributed to the recombination of STE from the free electrons to the STH states and the presence of DAP transition, respectively. Under illumination of 254 nm, the MSM UV detector of the β-Ga_2O_3 microbelt possessed DUV sensing properties. This work provides an available method to achieve ultra-wide bandgap semiconductor materials for micro-/nanophotonic applications.

Author Contributions: Conceptualization, Y.J.; methodology, Y.P.; software, Y.P.; validation, Y.P.; formal analysis, Y.P., Q.W. and Y.J.; investigation, Y.P.; Resources, L.W., R.Y., Y.Y. and L.Y.; data curation, Y.P.; writing—original draft preparation, Y.P.; writing—review and editing, Q.W. and Y.P.; supervision, Y.J.; project administration, Y.J.; funding acquisition, Y.J., Q.W. and L.Y. All authors have read and agreed to the published version of the manuscript.

Funding: The authors acknowledge the support from the Natural Science Foundation of China (12074019, 11674018), Beijing Municipal Education Commission (KM202110017003), and Ph.D. Program of Beijing Institute of Graphic Communication (27170123018).

Data Availability Statement: The data presented in this study are available from the corresponding author.

Conflicts of Interest: The authors declare no competing financial interest.

References

1. Xie, C.; Lu, X.; Tong, X.; Zhang, Z.; Liang, F.; Liang, L.; Luo, L.; Wu, Y. Recent progress in solar-blind deep-ultraviolet photodetectors based on inorganic ultrawide bandgap semiconductors. *Adv. Funct. Mater.* **2019**, *9*, 1806006. [CrossRef]
2. Chen, X.; Ren, F.; Gu, S.; Ye, J. Review of gallium-oxide-based solar-blind ultraviolet photodetectors. *Photonics Res.* **2019**, *4*, 381–415. [CrossRef]
3. Xu, J.; Zheng, W.; Huang, F. Gallium oxide solar-blind ultraviolet photodetectors: A review. *J. Mater. Chem. C* **2019**, *7*, 8753–8770. [CrossRef]
4. Fujita, S. Wide-bandgap semiconductor materials: For their full bloom. *Jpn. J. Appl. Phys.* **2015**, *54*, 030101. [CrossRef]
5. Deka Boruah, B. Zinc oxide ultraviolet photodetectors: Rapid progress from conventional to self-powered photodetectors. *Nanoscale Adv.* **2019**, *1*, 2059. [CrossRef] [PubMed]
6. Girolami, M.; Serpente, V.; Mastellone, M.; Tardocchi, M.; Rebai, M.; Xiu, Q.; Liu, J.; Sun, Z.; Zhao, Y.; Valentini, V.; et al. Self-powered solar-blind ultrafast UV-C diamond detectors with asymmetric Schottky contacts. *Carbon* **2022**, *189*, 27–36. [CrossRef]
7. Yu, Y.; Han, D.; Wei, H.; Tang, Z.; Luo, L.; Hong, T.; Shen, Y.; Zheng, H.; Wang, Y.; Wang, R.; et al. Aluminum Nitride Ultraviolet Light-Emitting Device Excited via Carbon Nanotube Field-Emission Electron Beam. *Nanomaterials* **2023**, *13*, 1067. [CrossRef]
8. Yang, J.; Liu, K.; Chen, X.; Shen, D. Recent advances in optoelectronic and microelectronic devices based on ultrawide-bandgap semiconductors. *Prog. Quant. Electron.* **2022**, *83*, 100397. [CrossRef]
9. Galazka, Z. β-Ga_2O_3 for wide-bandgap electronics and optoelectronics. *Semicond. Sci. Technol.* **2018**, *33*, 113001. [CrossRef]
10. Zhang, M.L.; Liu, Z.; Yang, L.L.; Yao, J.F.; Chen, J.; Zhang, J.; Wei, W.; Guo, Y.F.; Tang, W.H. β-Ga_2O_3-based power devices: A concise review. *Crystals* **2022**, *12*, 406. [CrossRef]
11. Liu, H.W.; Li, H.L.; Zhou, S.R.; Zhang, H.; Fan, S.Q.; Cui, Y.T.; Kong, C.Y.; Ye, L.J.; Xiong, Y.Q.; Li, W.J. Transport mechanism of enhanced performance in an amorphous/monoclinic mixed-phase Ga_2O_3 solar-blind deep ultraviolet photodetector. *Crystals* **2021**, *11*, 1111. [CrossRef]
12. Chen, M.N.; Zhang, Z.P.; Lv, Z.S.; Zhan, R.Z.; Chen, H.J.; Chen, J. Polycrystalline Ga_2O_3 nanostructure-based thin films for fast-response solar-blind photodetectors. *ACS Appl. Nano Mater.* **2022**, *5*, 351–360. [CrossRef]
13. Zhao, B.; Wang, F.; Chen, H.Y.; Wang, Y.P.; Jiang, M.M.; Fang, X.S.; Zhao, D.X. Solar-blind avalanche photodetector based on single ZnO-Ga_2O_3 core-shell microwire. *Nano Lett.* **2015**, *15*, 3988–3993. [CrossRef]
14. Jangir, R.; Porwal, S.; Tiwari, P.; Mondal, P.; Rai, S.K.; Srivastava, A.K.; Bhaumik, I.; Ganguli, T. Correlation between surface modification and photoluminescence properties of β-Ga_2O_3 nanostructures. *AIP Adv.* **2016**, *6*, 035120. [CrossRef]
15. Abdullah, Q.N.; Ahmed, R.A.; Ali, M.A.; Yam, K.F.; Hassan, Z.; Bououdina, M. Novel SnO_2-coated β-Ga_2O_3 nanostructures for room temperature hydrogen gas sensor. *Int. J. Hydrogen Energy* **2021**, *46*, 7000–7010. [CrossRef]
16. Mazeina, L.; Picard, Y.N.; Maximenko, S.I.; Perkins, F.K.; Glaser, E.R.; Twigg, M.E.; Freitas, J.A., Jr.; Prokes, S.M. Growth of Sn-doped β-Ga_2O_3 nanowires and Ga_2O_3-SnO_2 heterostructures for Gas sensing applications. *Cryst. Growth Des.* **2009**, *9*, 4471–4479. [CrossRef]
17. Hasan, S.; Jewel, M.U.; Crittenden, S.R.; Lee, D.; Avrutin, V.; Özgür, Ü.; Morkoç, H.; Ahmad, I. MOCVD-grown β-Ga_2O_3 as a Gate Dielectric on AlGaN/GaN-Based Heterojunction Field Effect Transistor. *Crystals* **2023**, *13*, 231. [CrossRef]
18. Wang, H.; Yang, J.W.; Wang, A.Q.; Wang, Y.; Han, N.; Yang, J.; Chen, Y.F. Controllable Ga/Ga_2O_3 nanowire growth at high temperatures enabled by Au and Pd quantum dot catalysts. *Cryst. Growth Des.* **2022**, *22*, 6183–6189. [CrossRef]
19. Gonzalo, A.; Nogales, E.; Lorenz, K.; Víllora, E.G.; Shimamura, K.; Piqueras, J.; Méndez, B. Raman and cathodoluminescence analysis of transition metal ion implanted Ga_2O_3 nanowires. *J. Lum.* **2017**, *191*, 56–60. [CrossRef]
20. Kumar, S.; Sarau, G.; Tessarek, C.; Bashouti, M.Y.; Hähnel, A.; Christiansen, S.; Singh, R. Study of iron-catalysed growth of β-Ga_2O_3 nanowires and their detailed characterization using TEM, Raman and cathodoluminescence techniques. *J. Phys. D Appl. Phys.* **2014**, *47*, 435101. [CrossRef]
21. Feng, Q.J.; Li, T.T.; Li, F.; Li, Y.Z.; Shi, B.; Gao, C.; Wang, D.Y.; Liang, H.W. Catalyst-free growth of single crystalline β-Ga_2O_3 microbelts on patterned sapphire substrates. *J. Cryst. Growth* **2019**, *509*, 91–95. [CrossRef]
22. Wang, Y.F.; Li, L.; Wang, H.B.; Su, L.X.; Chen, H.Y.; Bian, W.P.; Ma, J.G.; Li, B.S.; Liu, Z.G.; Shen, A.D. An ultrahigh responsivity self-powered solar-blind photodetector based on a centimeter-sized β-Ga_2O_3/polyaniline heterojunction. *Nanoscale* **2020**, *12*, 1406–1413. [CrossRef]
23. Wang, Q.; Yan, Y.Z.; Zeng, Y.; Lu, Y.; Chen, L.; Jiang, Y.J. Free-standing undoped ZnO microtubes with rich and stable shallow acceptors. *Sci. Rep.* **2016**, *6*, 27341. [CrossRef]
24. Pan, Y.M.; Yan, Y.Z.; Wang, Q.; Yang, L.X.; Zhang, X.G.; Tang, L.; Xing, C.; Chen, F.; Jiang, Y.J. Efficient defect control of zinc vacancy in undoped ZnO microtubes for optoelectronic applications. *J. Appl. Phys.* **2022**, *131*, 105105. [CrossRef]

25. Zhang, X.G.; Chen, F.; Jiang, Y.J.; Yan, Y.Z.; Yang, L.X.; Yang, L.T.; Wang, X.H.; Yu, C.L.; Hu, L.N.; Dai, Y.H.; et al. Graphene oxide modified microtubular ZnO antibacterial agents for a photocatalytic filter in a facial mask. *ACS Appl. Nano Mater.* **2022**, *5*, 16332–16343.
26. Liao, Y.M.; Yan, Y.Z.; Yang, L.X.; Pan, Y.M.; Lu, Y.; Chen, F.; Wang, Q.; Jiang, Y.J. Free-standing $In_2O_3(ZnO)_m$ superlattice microplates grown by optical vapor supersaturated precipitation. *J. Mater. Sci.* **2021**, *56*, 13723–13735. [CrossRef]
27. Gatsi, N.C.; Mhlongo, G.H.; Moloto, N.; Erasmus, R.M.; Mashazi, P.; Nyokong, T.; Ntwaeaborwa, O.M. Hierarchically-ordered nanorods of Ga_2O_3 derived from microwave-assisted hydrothermal approach: Investigation of calcination-induced structural evolution and optical behavior. *Mater. Today Commun.* **2022**, *33*, 104808. [CrossRef]
28. Zhao, J.J.; Qin, B.H.; Liu, L.H.; Liang, C.M.; Zhang, Y.P.; Yang, W.J.; Wang, H.Y. Enhanced low-temperature response of Ga_2O_3-based oxygen sensor by modulating the surficial micro-nano structures. *Sens. Actuators B Chem.* **2023**, *378*, 133180. [CrossRef]
29. Hou, X.H.; Zhao, X.L.; Zhang, Y.; Zhang, Z.F.; Liu, Y.; Qin, Y.; Tan, P.J.; Chen, C.; Yu, S.J.; Ding, M.F.; et al. High-performance harsh-environment-resistant GaO_X solar blind photodetectors via defect and doping engineering. *Adv. Mater.* **2022**, *34*, 2106923. [CrossRef]
30. Chang, P.C.; Fan, Z.Y.; Tseng, W.Y.; Rajagopal, A.; Lu, G.J. β-Ga_2O_3 nanowires: Synthesis, characterization, and *p*-channel field-effect transistor. *Appl. Phys. Lett.* **2005**, *87*, 222102. [CrossRef]
31. Frodason, Y.K.; Johansen, K.M.; Vines, L.; Varley, J.B. Self-trapped hole and impurity-related broad, luminescence in β-Ga_2O_3. *J. Appl. Phys.* **2020**, *127*, 75701. [CrossRef]
32. Yamaoka, S.; Furukawa, Y.; Nakayama, M. Initial process of photoluminescence dynamics of self-trapped excitons in a β-Ga_2O_3 single crystal. *Phys. Rev. B* **2017**, *95*, 094304. [CrossRef]
33. Varley, J.B.; Janotti, A.; Franchini, C.; Van de Walle, C.G. Role of self-trapping in luminescence and *p*-type conductivity of wide-band-gap oxides. *Phys. Rev. B* **2012**, *85*, 081109. [CrossRef]
34. Nogales, E.; García, J.A.; Méndez, B.; Piqueras, J. Red luminescence of Cr in β-Ga_2O_3 nanowires. *J. Appl. Phys.* **2007**, *101*, 033517. [CrossRef]
35. Sharma, S.; Sunkara, M.K. Direct synthesis of gallium oxide tubes, nanowires, and nanopaintbrushes. *J. Am. Chem. Soc.* **2002**, *124*, 12288–12293. [CrossRef]
36. Wu, X.C.; Song, W.H.; Huang, W.D.; Pu, M.H.; Zhao, B.; Sun, Y.P.; Du, J.J. Crystalline gallium oxide nanowires: Intensive blue light emitter. *Chem. Phys. Lett.* **2000**, *328*, 5–9. [CrossRef]
37. Zheng, Z.Y.; Liu, K.W.; Cheng, Z.; Qiao, B.S.; Chen, X.; Zhou, C.; Yang, J.L.; Ai, Q.; Zhu, Y.X.; Li, B.H.; et al. Single β-Ga_2O_3 microbelt solar-blind photodetector with high specific detectivity, high rejection ratio and fast speed. *J. Phys. D Appl. Phys.* **2022**, *55*, 365107. [CrossRef]
38. Altuntas, H.; Donmez, I.; Ozgit-Akgun, C.; Biyikli, N. Electrical characteristics of β-Ga_2O_3 thin films grown by PEALD. *J. Alloys Compd.* **2014**, *593*, 190–195. [CrossRef]
39. Onuma, T.; Fujioka, S.; Yamaguchi, T.; Itoh, Y.; Higashiwaki, M.; Sasaki, K.; Masui, T.; Honda, T. Polarized Raman spectra in β-Ga_2O_3 single crystals. *J. Cryst. Growth* **2014**, *401*, 330–333. [CrossRef]
40. Zhang, K.; Xu, Z.W.; Zhao, J.L.; Wang, H.; Hao, J.M.; Zhang, S.N.; Cheng, H.J.; Dong, B. Temperature-dependent Raman and photoluminescence of β-Ga_2O_3 doped with shallow donors and deep acceptors impurities. *J. Alloys Compd.* **2021**, *881*, 160665. [CrossRef]
41. Rao, R.; Rao, A.M.; Xu, B.; Dong, J.; Sharma, S.; Sunkara, M.K. Blueshifted Raman scattering and its correlation with the [110] growth direction in gallium oxide nanowires. *J. Appl. Phys.* **2005**, *98*, 94312. [CrossRef]
42. Dohy, D.; Lucazeau, G.; Revcolevschi, A. Raman spectra and valence force field of single-crystalline β-Ga_2O_3. *J. Solid State Chem.* **1982**, *45*, 180–192. [CrossRef]
43. Ilhom, S.; Mohammad, A.; Shukla, D.; Grasso, J.; Willis, G.B.; Okyay, A.K.; Biyikli, N. Low-temperature as-grown crystalline β-Ga_2O_3 films via plasma-enhanced atomic layer deposition. *ACS Appl. Mater. Interfaces* **2021**, *13*, 8538–8551.
44. Yadav, M.K.; Mondal, A.; Das, S.; Sharma, S.K.; Bag, A. Impact of annealing temperature on band-alignment of PLD grown Ga_2O_3/Si (100) heterointerface. *J. Alloys Compd.* **2020**, *819*, 153052. [CrossRef]
45. Fu, B.; Mu, W.X.; Li, Y.; Shi, Y.J.; Li, Y.B.; Jia, Z.T.; Tao, X.T. Investigation of the blue color center in β-Ga_2O_3 crystals by the EFG method. *CrystEngComm* **2021**, *23*, 8360. [CrossRef]
46. Chen, R.R.; Wang, D.; Liu, J.; Feng, B.; Zhu, H.Y.; Han, X.Y.; Luan, C.N.; Ma, J.; Xiao, H.D. Ta-Doped Ga_2O_3 epitaxial films on porous p-GaN substrates: Structure and self-powered solar-blind photodetectors. *Cryst. Growth Des.* **2022**, *22*, 5285–5292. [CrossRef]
47. He, C.R.; Guo, D.Y.; Chen, K.; Wang, S.L.; Shen, J.Q.; Zhao, N.; Liu, A.P.; Zheng, Y.Y.; Li, P.G.; Wu, Z.P.; et al. α-Ga_2O_3 nanorod array-Cu_2O microsphere p-n junctions for self-powered spectrum-distinguishable photodetectors. *ACS Appl. Nano Mater.* **2019**, *7*, 4095–4103. [CrossRef]
48. Zhang, Y.Q.; Wang, Y.F.; Fu, R.P.; Ma, J.G.; Xu, H.Y.; Li, B.S.; Liu, Y.C. High performance solar-blind ultraviolet photodetector based on ITO/β-Ga_2O_3 heterostructure. *J. Phys. D Appl. Phys.* **2022**, *55*, 324002. [CrossRef]
49. Zhou, W.; Xia, C.T.; Sai, Q.L.; Zhang, H.Z. Controlling *n*-type conductivity of β-Ga_2O_3 by Nb doping. *Appl. Phys. Lett.* **2017**, *111*, 242103. [CrossRef]

50. Tang, H.L.; He, N.T.; Zhu, Z.C.; Gu, M.; Liu, B.; Xu, J.; Xu, M.X.; Chen, L.; Liu, J.L.; Ouyang, X.P. Temperature-dependence of X-ray excited luminescence of β-Ga_2O_3 single crystals. *Appl. Phys. Lett.* **2019**, *115*, 71904. [CrossRef]
51. Harwig, T.; Kellendonk, F. Some Observations on the photoluminescence of doped β-Galliumsesquioxide. *J. Solid State Chem.* **1978**, *24*, 255–263. [CrossRef]
52. Harwig, T.; Kellendonk, F.; Slappende, S. The ultraviolet luminescence of β-galliumsesquioxide. *J. Phys. Chem. Solids* **1978**, *39*, 673–680. [CrossRef]
53. Onuma, T.; Fujioka, S.; Yamaguchi, T.; Higashiwaki, M.; Sasaki, K.; Masui, T.; Honda, T. Correlation between blue luminescence intensity and resistivity in β-Ga_2O_3 single crystals. *Appl. Phys. Lett.* **2013**, *103*, 41910. [CrossRef]
54. Gao, H.T.; Muralidharan, S.; Pronin, N.; Karim, M.R.; White, S.M.; Asel, T.; Foster, G.; Krishnamoorthy, S.; Rajan, S.; Cao, L.R.; et al. Optical signatures of deep level defects in Ga_2O_3. *Appl. Phys. Lett.* **2018**, *112*, 242102. [CrossRef]
55. Onuma, T.; Nakata, Y.; Sasaki, K.; Masui, T.; Yamaguchi, T.; Honda, T.; Kuramata, A.; Yamakoshi, S.; Higashiwaki, M. Modeling and interpretation of UV and blue luminescence intensity in β-Ga_2O_3 by silicon and nitrogen doping. *J. Appl. Phys.* **2018**, *1124*, 75103. [CrossRef]
56. Ho, D.Q.; Frauenheim, T.; Deák, P. Origin of photoluminescence in β-Ga_2O_3. *Phys. Rev. B* **2018**, *97*, 115163. [CrossRef]
57. Wang, S.L.; Sun, H.L.; Wang, Z.; Zeng, X.H.; Ungar, G.; Guo, D.Y.; Shen, J.Q.; Li, P.G.; Liu, A.P.; Li, C.R.; et al. In situ synthesis of monoclinic β-Ga_2O_3 nanowires on flexible substrate and solar-blind photodetector. *J. Alloys Compd.* **2019**, *787*, 133–139. [CrossRef]
58. Han, N.; Wang, F.Y.; Yang, Z.X.; Yip, S.P.; Dong, G.F.; Lin, H.; Fang, M.; Hung, T.; Ho, J.C. Low-temperature growth of highly crystalline β-Ga_2O_3 nanowires by solid-source chemical vapor deposition. *Nanoscale Res. Lett.* **2014**, *9*, 347. [CrossRef] [PubMed]
59. Ding, W.; Meng, X. High performance solar-blind UV detector based on β-Ga_2O_3/GaN nanowires heterojunction. *J. Alloys Compd.* **2021**, *866*, 157564. [CrossRef]
60. Girolami, M.; Bosi, M.; Serpente, V.; Mastellone, M.; Seravalli, L.; Pettinato, S.; Salvatori, S.; Trucchi, M.D.; Fornari, R. Orthorhombic undoped κ-Ga_2O_3 epitaxial thin films for sensitive, fast, and stable direct X-ray detectors. *J. Mater. Chem. C* **2023**, *11*, 3759. [CrossRef]

Disclaimer/Publisher's Note: The statements, opinions and data contained in all publications are solely those of the individual author(s) and contributor(s) and not of MDPI and/or the editor(s). MDPI and/or the editor(s) disclaim responsibility for any injury to people or property resulting from any ideas, methods, instructions or products referred to in the content.